

# Microscale Investigations of Ni Uptake by Cement Using a Combination of Scanning Electron Microscopy and Synchrotron-Based Techniques

M. VESPA,<sup>\*,†,‡</sup> R. DÄHN,<sup>†</sup> E. GALLUCCI,<sup>§</sup> D. GROLIMUND,<sup>†</sup> E. WIELAND,<sup>†</sup> AND A. M. SCHEIDEGGER<sup>†,‡</sup>

Laboratory for Waste Management, Paul Scherrer Institute, 5232 Villigen PSI, Switzerland, Department of Environmental Sciences, Swiss Federal Institute of Technology (ETH), Zürich, Switzerland, and Construction Materials Laboratory, IMX, Ecole Polytechnique Fédérale de Lausanne (EPFL), 1015 Lausanne, Switzerland

Cement is used to condition waste materials and for the construction and backfilling of repositories for low- and intermediate-level radioactive waste. In this study, Ni uptake by hardened cement paste has been investigated with the aim of improving our understanding of the immobilization process of Ni(II) in cement on the microscale. Information on the cement microstructure, Ni distribution, Ni concentration, and speciation of the Ni phases formed in the cement system and their association with specific cement minerals has been gained by using scanning electron microscopy (SEM) and synchrotron-based  $\mu$ -X-ray fluorescence ( $\mu$ -XRF) and  $\mu$ -X-ray absorption spectroscopy ( $\mu$ -XAS). The Ni-doped samples were prepared at a water/cement ratio of 0.4 using a sulfate-resisting Portland cement and were hydrated for 30 days. The metal loadings of the system were varied from 50 up to 5000 mg/kg. SEM investigations show that for all metal loadings the Ni phases form rims around inner-calcium silicate hydrates, suggesting a direct association with this cement phase. The  $\mu$ -XAS measurements further reveal that a mixture of Ni phases form at Ni-enriched regions. Data analysis indicates that Ni(II) is predominantly immobilized in a layered double hydroxide-type phase (Ni–Al LDH) and only to a minor extent precipitates as Ni-hydroxides ( $\alpha$ -Ni(OH)<sub>2</sub> and  $\beta$ -Ni(OH)<sub>2</sub>). At 50 mg/kg Ni loading, however, the  $\mu$ -XAS measurements suggest the presence of an additional Ni species. In the latter system Ni–Al LDH is found in Ni-rich regions, whereas at Ni-poor regions an unknown species is formed.

## Introduction

Cement-based materials have been used worldwide for stabilizing hazardous and radioactive wastes to prevent or

lower the mobility of contaminants in the environment that are present in the waste matrices. The long-term disposal of cement-stabilized hazardous waste is associated with land-filling of these waste forms (e.g., ref 1), whereas deep geological disposal is foreseen for some categories of cement-stabilized radioactive waste (2).

Thus, a molecular-level understanding of the processes governing the immobilization of heavy metals in hydrating cement is essential for long-term predictions of the environmental impact of cement-stabilized waste forms. From a chemical standpoint, hardened cement paste (HCP) is a very heterogeneous material with discrete particles in the nano- to micrometer size range. The material consists of mainly calcium (aluminum) silicate hydrates (C–(A)–S–H), portlandite (calcium hydroxide), calcium aluminates, and calcium ferrites. The immobilization potential of HCP originates from its selective binding properties for metal cations and anions (e.g., ref 3). Therefore, it appears that immobilization processes in cement systems are highly specific with respect to the mineral components and mechanisms involved.

Ni is an important contaminant in waste materials, generated in various industrial processes, such as electricity production in nuclear power plants. In the past, only few X-ray absorption spectroscopic (XAS) studies have been reported on the Ni uptake by cement. Investigations of Ni sorption onto hydrated Portland cement revealed that a mixture of Ni(OH)<sub>2</sub> and Ni–Al layered double hydroxide (Ni–Al LDH, [M<sup>II</sup><sub>1-x</sub>M<sup>III</sup><sub>x</sub>(OH)<sub>2</sub>]<sup>x+</sup>(A<sup>n-</sup>)<sub>x/n</sub>·yH<sub>2</sub>O) phases form in these systems (4). In a recent study, Vespa et al. (5) investigated the Ni speciation during cement hydration using XAS on powdered Ni-doped cement samples (bulk-XAS). The varied experimental parameters were hydration time, anions added to the system, water/cement (w/c) ratio, and Ni concentration. The study revealed the predominant formation of Ni–Al LDH in the hydrating cement system (500 and 5000 mg/kg Ni loadings) with small amounts of Ni-hydroxide phases ( $\alpha$ -Ni(OH)<sub>2</sub> and  $\beta$ -Ni(OH)<sub>2</sub>). The study further showed that the amount of Ni–Al LDH increases as a function of hydration time, whereas  $\alpha$ -Ni(OH)<sub>2</sub> decreases and  $\beta$ -Ni(OH)<sub>2</sub> remains constant. These findings were independent of the anions added to the system or the w/c ratio. The only exception was found in the sample with the lowest Ni loading (50 mg/kg), where the Ni speciation was not dominated by the presence of Ni–Al LDH and Ni-hydroxides.

The goal of this study was to investigate the Ni uptake by HCP on the microscale and to further investigate the influence of the inherent heterogeneity of the cement matrix on the Ni speciation. To achieve this goal, scanning electron microscopy (SEM),  $\mu$ -synchrotron-X-ray fluorescence ( $\mu$ -XRF), and  $\mu$ -XAS were combined. SEM allows spatially resolved information on the microstructure of the clinker, that is, nonhydrated cement minerals, and hydrated cement phases as well as associations of the Ni phases with specific cement minerals to be gained. Additionally,  $\mu$ -XRF allows larger areas to be investigated and is therefore well suited to gain an overview of the Ni distribution. To determine the chemical speciation of Ni at selected regions of the cement matrix,  $\mu$ -XAS was employed. The knowledge acquired through this study will allow the development of a molecular-level understanding of the Ni uptake processes in cement. Moreover, the comparison between the microscale investigation and the bulk-XAS measurements (5) will allow identification of the relevant Ni species formed in the cement matrix.

\* Corresponding author phone: +41-56-310-2966; fax: +41-56-310-4595; e-mail: marika.vespa@psi.ch.

<sup>†</sup> Paul Scherrer Institute.

<sup>‡</sup> Swiss Federal Institute of Technology.

<sup>§</sup> Ecole Polytechnique Fédérale de Lausanne.

## Materials and Methods

**Sample Preparation.** The cement samples were prepared from a commercial sulfate-resisting Portland cement (CEM I 52.5 N HTS, Lafarge, France) used to condition radioactive waste in Switzerland. Ni-doped HCP was prepared by mixing a  $\text{Ni}(\text{NO}_3)_2$  solution with unhydrated cement. The metal salt was dissolved in deionized water to obtain three stock solutions with concentrations of 0.003, 0.03, and 0.3 mol/L ( $\text{pH} = 4.5\text{--}5$ ). The solutions were mixed with the unhydrated cement at a w/c ratio of 0.4, using a standard procedure (5). The final metal concentrations of the pastes were 50 ( $\text{Ni}_{\text{cem}_50}$ ), 500 ( $\text{Ni}_{\text{cem}_500}$ ), and 5000 ( $\text{Ni}_{\text{cem}_5000}$ ) mg/kg dry HCP. The cement pastes were poured into plexiglass molds, which were closed with polyethylene lids, and were hydrated for 30 days. The samples were stored in closed containers at room temperature at 100% relative humidity. Upon hydration, the cylinders were cut into several slices of  $\sim 1$  cm thickness and were dried in the glovebox in a dry  $\text{N}_2$  atmosphere. Some slices were impregnated and polished for the preparation of thin sections, which were employed for SEM and  $\mu\text{-XRF}/\mu\text{-XAS}$  measurements.

**Scanning Electron Microscopic Investigations.** The SEM experiments were conducted at the Laboratory for Construction Materials (IMX), Ecole Polytechnique Fédérale de Lausanne (EPFL), using an FEI Quanta 200 microscope and at the Laboratory for Materials Behaviour (LWV), Paul Scherrer Institute (PSI), using a Zeiss DSM 962 microscope. The FEI microscope was operated at an accelerating voltage of 15 kV and at a beam current of 100  $\mu\text{A}$ , whereas the Zeiss was operated at an accelerating voltage of 20 kV and at a beam current of 76  $\mu\text{A}$ . The FEI microscope is equipped with a solid-state detector, whereas the Zeiss is equipped with a photomultiplier for backscattering electron (BSE) images. Both microscopes are equipped with a Si(Li)-detector for energy-dispersive microanalysis (EDS). The sample-volume probed was  $\sim 1 \mu\text{m}^3$ .

BSE generates a specific phase contrast thanks to which minerals can be identified according to their brightness in the image. The minerals with the greatest average atomic number show the brightest contrast, whereas those with the lower atomic number show darker contrast. This allows the mineral components in the microstructure, both of unreacted clinker and hydrated cement phases, to be distinguished on the basis of their gray level. As a consequence, phases containing high concentrations of light elements such as calcium, hydrogen, and oxygen (i.e., C–S–H) will be darker than other phases predominantly consisting of heavier elements such as Ni, Fe, or oxides such as  $\text{Ca}_2\text{SiO}_4$  or  $\text{Ca}_3\text{SiO}_5$ .

The BSE images and elemental distribution maps, using an EDS system, were performed on the same polished thin sections used for the microspectroscopic investigations.

**$\mu\text{-XRF}/\mu\text{-XAS}$  Data Collection and Reduction.**  $\mu\text{-XRF}/\mu\text{-XAS}$  data were collected on beamline 10.3.2 ALS/USA (6). The monochromator angle was calibrated by assigning the energy of 8333 eV to the first inflection point of the K-edge absorption spectrum of Ni metal foil. The  $\mu\text{-XRF}/\mu\text{-XAS}$  measurements were collected at room temperature in fluorescence mode using a seven-element Ge-solid-state detector with a beam size of  $\sim 5 \times 5 \mu\text{m}^2$ . The  $\mu\text{-XRF}$  maps were obtained by scanning the sample under the monochromatic beam at the energy of 10 000 eV with a pixel size of  $5 \times 5 \mu\text{m}^2$ .

Data reduction was performed by standard procedures (see Supporting Information) using the WinXAS 3.1 software package (7). Several reference spectra ( $\beta\text{-Ni}(\text{OH})_2$ ,  $\alpha\text{-Ni}(\text{OH})_2$ , synthetic Ni–Al LDH ( $\text{Ni}:\text{Al}$ , 2:1)  $\text{Ni}_2\text{Al}(\text{OH})_6(\text{CO}_3)_{1/2}$  (8), Ni-phyllsilicate, neoformed Ni–Al LDH formed from Ni-doped

pyrophyllite) collected at the SNBL/ESRF, France, were used to identify the Ni species in the cement matrix (5).

## Results and Discussion

**Distribution and Speciation of the Ni Phases.** BSE-imaging allows minerals of different compositions to be identified. Figure 1a–c shows selected BSE images of the Ni-doped HCP sample at a w/c = 0.4, hydrated for 30 days and with a metal concentration of 5000 mg/kg. In the first BSE image (Figure 1a), the nonhydrated clinker mineral phases, belite ( $\text{Ca}_2\text{SiO}_4$ ) and alite ( $\text{Ca}_3\text{SiO}_5$ ), can be identified. Belite and alite are the major clinker phases in cement (9) with particles ranging in size between a few microns and tens of microns. During hydration, which starts upon addition of water to cement, alite and belite decompose to form calcium silicate hydrates (C–S–H) and calcium hydroxide (portlandite). C–S–H is the most abundant hydrated cement phase and confers most of its properties to the HCP. It precipitates under two main forms: inner-C–S–H and outer-C–S–H. The inner-C–S–H gradually fills up the space originally occupied by alite grains. After some time of hydration, most of the alite grains are surrounded by a rim of inner-C–S–H (white frame in Figure 1a) varying in thickness. In some cases, alite was completely reacted and replaced by inner-C–S–H (black frame in Figure 1a). On the other hand, the outer-C–S–H (darker gray area indicated in Figure 1a and c) fills the porous space of the hydrated cement originally occupied by water. The outer-C–S–H is generally less dense than the inner-C–S–H and is finely intermixed with portlandite and several other minor hydrated phases, such as ettringite ( $\text{Ca}_6\text{Al}_2(\text{SO}_4)_3(\text{OH})_{12} \cdot 26\text{H}_2\text{O}$ ). The bright rims around inner-C–S–H phases found in Ni-doped HCP (red dashed area in Figure 1c) were not observed in the non-doped HCP. The elemental distribution maps displayed in Figure 1d–i show that Ni is accumulated in these bright rims. The Ni rim shown in Figure 1 has a thickness of  $\sim 5 \mu\text{m}$  and a diameter of  $\sim 20\text{--}50 \mu\text{m}$ . This is an unusually large rim, which has been rarely observed in the investigated cement matrix. In general, rims of a few hundred nanometers up to a few microns thickness and up to  $\sim 10 \mu\text{m}$  in diameter have been observed, as shown in Figure 2a–i. Although, Figure 1 and Figure 2 show rims with different sizes, they display common features. The BSE images (Figure 1a–c, Figure 2a–c) show that the bright Ni-rich rims form around inner-C–S–H. The elemental distribution maps (Figure 1d–i, Figure 2d–i) reveal that Ni anticorrelates with Ca and Si, whereas correlation with Al and O is found. The Ca–Si anticorrelation is less obvious in Figure 2 because of the large amount of small alite grains totally reacted to inner-C–S–H, which are surrounded by a relatively thin Ni rim (Figure 2c–d red circle). Furthermore, in between these grains, outer-C–S–H has precipitated. The Ni–Al correlation is also less evident because of high Al concentrations. The significant correlation of Al with Fe, and to a lesser extent with Ca, visible at this particular spot (Figure 2), suggests the presence of ferrite ( $4\text{CaO} \cdot \text{Al}_2\text{O}_3 \cdot \text{Fe}_2\text{O}_3$ ) or hydrated products of ferrite. No correlation of Ni with Fe was observed.

The EDS analyses of selected spots on the Ni rims confirm the correlation between Ni and Al. The Al concentrations vary between  $\sim 1\text{--}3$  wt %, whereas the Ni concentrations range between  $\sim 2\text{--}13$  wt % for thinner (Table S1, analyses f–h and l–q, Supporting Information, indicated in Figure 1b and Figure 2b) and  $\sim 22\text{--}28$  wt % for thicker rims (Table S1, analyses c–e indicated in Figure 1b). The observed Ni:Al ratio is consistent with data published recently by Peltier et al. (10). Further EDS analyses of selected regions show that Ni is present neither in alite (Table S1, analyses i and k indicated in Figure 2b) nor in inner-C–S–H or portlandite (Table S1, analyses a, b indicated in Figure 1b, and analysis j indicated in Figure 2b). However, the EDS analyses show that Ca ( $\sim 10\text{--}30$  wt %) and Si ( $\sim 2\text{--}10$  wt %) are present in



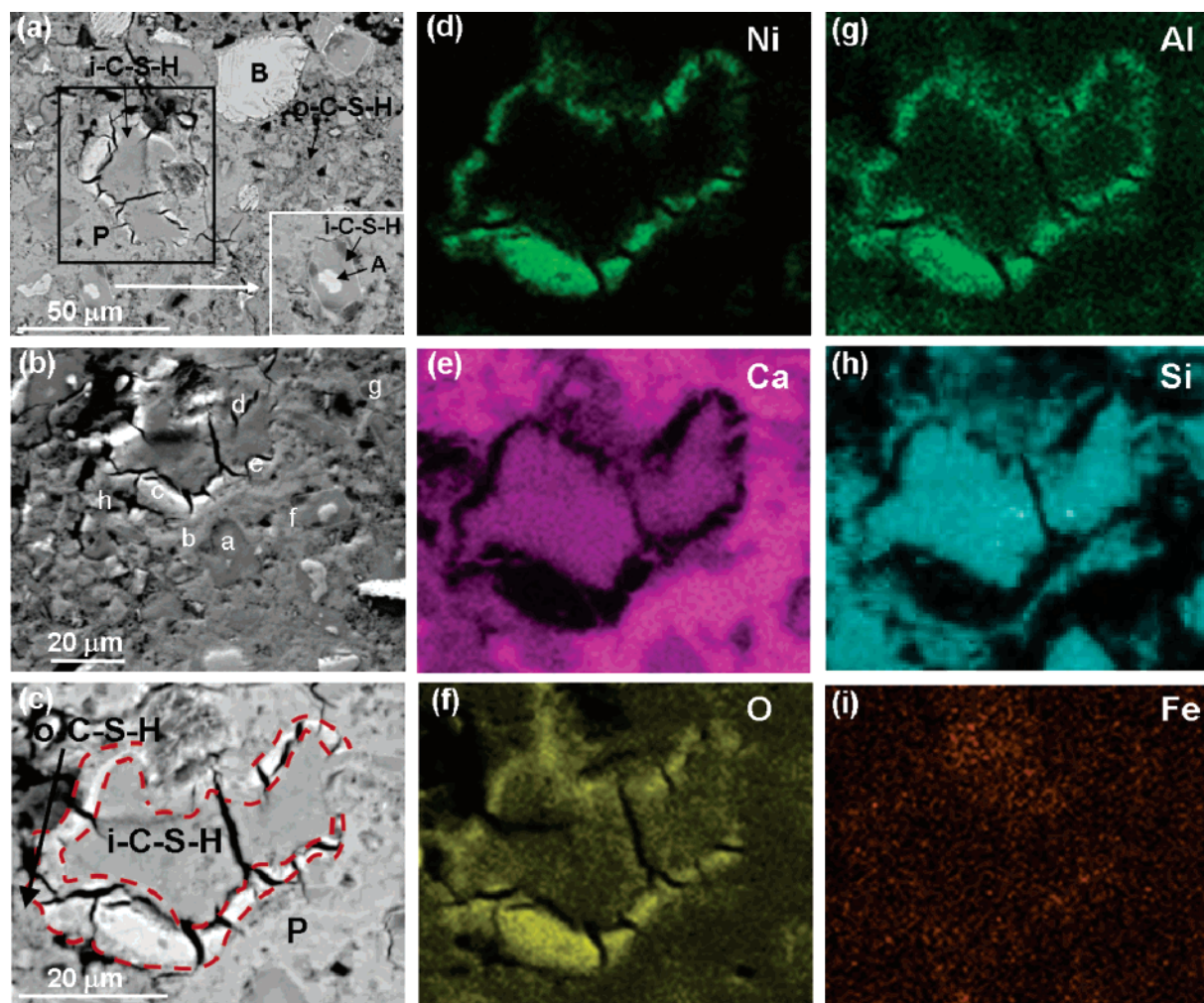


**FIGURE 1.** BSE images (a–c) and SEM/EDS elemental distribution maps (d–i) of a Ni-rich region from the  $\text{Ni}(\text{NO}_3)_2$ -doped HCP sample with a water/cement ratio of 0.4 and a final metal concentration of 5000 mg/kg hydrated for 30 days. The white frame in a shows the enlarged region indicated by the arrow. In the enlarged picture, an alite crystal is observed with the rim of inner-C–S–H. The black frame in a represents the 90° anticlockwise flipped image of the two BSE images observed in b and c, representing the Ni-rich region, and the SEM/EDS maps (d–i). In the SEM/EDS maps (d–i), brighter colors represent higher concentrations, whereas darker colors represent lower concentrations. The lowercase letters a–h in b indicate the regions of the SEM/EDS single spot analyses. The red dashed area in c represents the Ni-rich region. Notations: B = belite ( $\text{Ca}_2\text{SiO}_4$ ), A = alite ( $\text{Ca}_3\text{SiO}_5$ ), P = portlandite ( $\text{Ca}(\text{OH})_2$ ), i-C–S–H = inner-calcium silicate hydrate, o-C–S–H = outer-C–S–H.

several percentages in the Ni-rich rims (Table S1, analyses c–h and l–q indicated in Figure 1b and Figure 2b). This seems to be in contrast with the elemental distribution maps, which revealed an anticorrelation of Ni with Ca and Si. Nevertheless, one must bear in mind that distribution maps are relative measurements based on the elemental concentration rather than on absolute measurements. Finally, the EDS analyses indicate that further elements, which are present in trace concentrations in the cement matrix (Fe, S, Sr, Mg, Na, K, Cr, Cl, Table S1), are completely absent in the Ni rims.

A tentative explanation for the formation of Ni-rich rims around alite grains can be given by considering some specific features of this mineral. First, alite dissolves much faster than belite, thus acting as a reactive zone in the cement matrix. Second, traces of Mg and Al are predominantly associated with alite (Mg = 0.35 wt % (9, 11)). Mg is an important constituent of hydrotalcite-like phases ( $[\text{Mg}_{1-x}\text{Al}_x(\text{OH})_2]^{x+}(\text{A}^{n-})_{x/n} \cdot y\text{H}_2\text{O}$ ), which were also observed in the hydrating cement matrix (9) and belong to the group of the LDH-phases. Aluminate phases ( $3\text{CaO} \cdot \text{Al}_2\text{O}_3$ ) were found to readily dissolve, thereafter, being the main source of Al in the cement matrix. However, Mg was not observed to be

present in the aluminate phases (11). Therefore, it is speculated that Mg could play an important role in the formation of Ni–Al LDH and, thus, in the Ni accumulation in the reactive zones around alite. Mg may be bound in the neoformed Ni–Al LDH but at concentrations well below the detection limit of the techniques used in the present study.

The regions studied by SEM were also investigated by  $\mu$ -XRF. Figure 3a shows the elemental distribution of Ni, Ca, and Fe in a  $\sim 800 \times 1000 \mu\text{m}^2$  overview map. The region shows a heterogeneous distribution of these elements. All elements reveal higher and lower concentrated regions. The regions with high Ca or Fe concentrations represent the clinker minerals, whereas the lower concentrated regions represent the hydrated cement phases. Ni shows an anticorrelation with Ca and no correlation with Fe, consistent with the SEM/EDS results. The SEM region outlined in Figure 1 represents region 1 on the  $\mu$ -XRF map (Figure 3a). The area outlined in Figure 2 represents region 2 (Figure 3a). The observation that  $\mu$ -XRF maps display Ni “spotslike” instead of “rims” is a consequence of the penetration depth. The higher penetration depth of the synchrotron X-ray beam ( $\sim$ hundred microns) compared to the penetration depth of an electron beam (a few microns) caused the fluorescence signal to smear



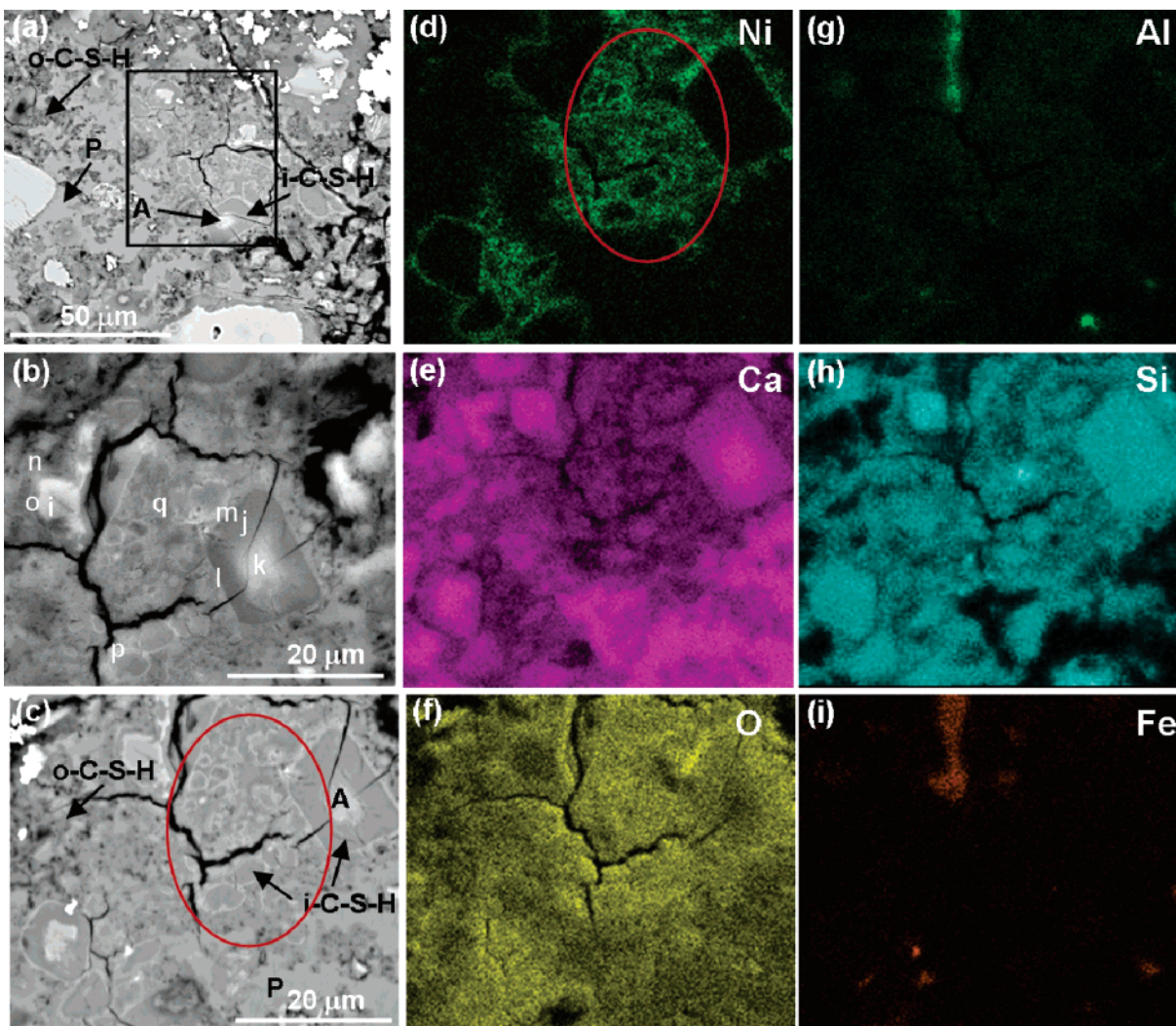


**FIGURE 2.** BSE images (a–c) and SEM/EDS elemental distribution maps (d–i) of a further Ni-rich region with relatively fine rims (1–2  $\mu\text{m}$ ) of the  $\text{Ni}(\text{NO}_3)_2$ -doped HCP sample with a water/cement ratio of 0.4 and a final metal concentration of 5000 mg/kg hydrated for 30 days. The black frame in a represents the 90° anticlockwise flipped image of the other two BSE images observed in b and c, representing the Ni-rich area, and the SEM/EDS maps (d–i). In the SEM/EDS maps (d–i), brighter colors represent higher concentrations, whereas darker colors represent lower concentrations. The lowercase letters i–p in b indicate the regions of the SEM/EDS single spot analyses. Notations: A = alite ( $\text{Ca}_3\text{SiO}_5$ ), P = portlandite ( $\text{Ca}(\text{OH})_2$ ), i-C-S-H = inner-calcium silicate hydrate, o-C-S-H = outer-C-S-H. The red circles in c and d indicate features explained in the text.

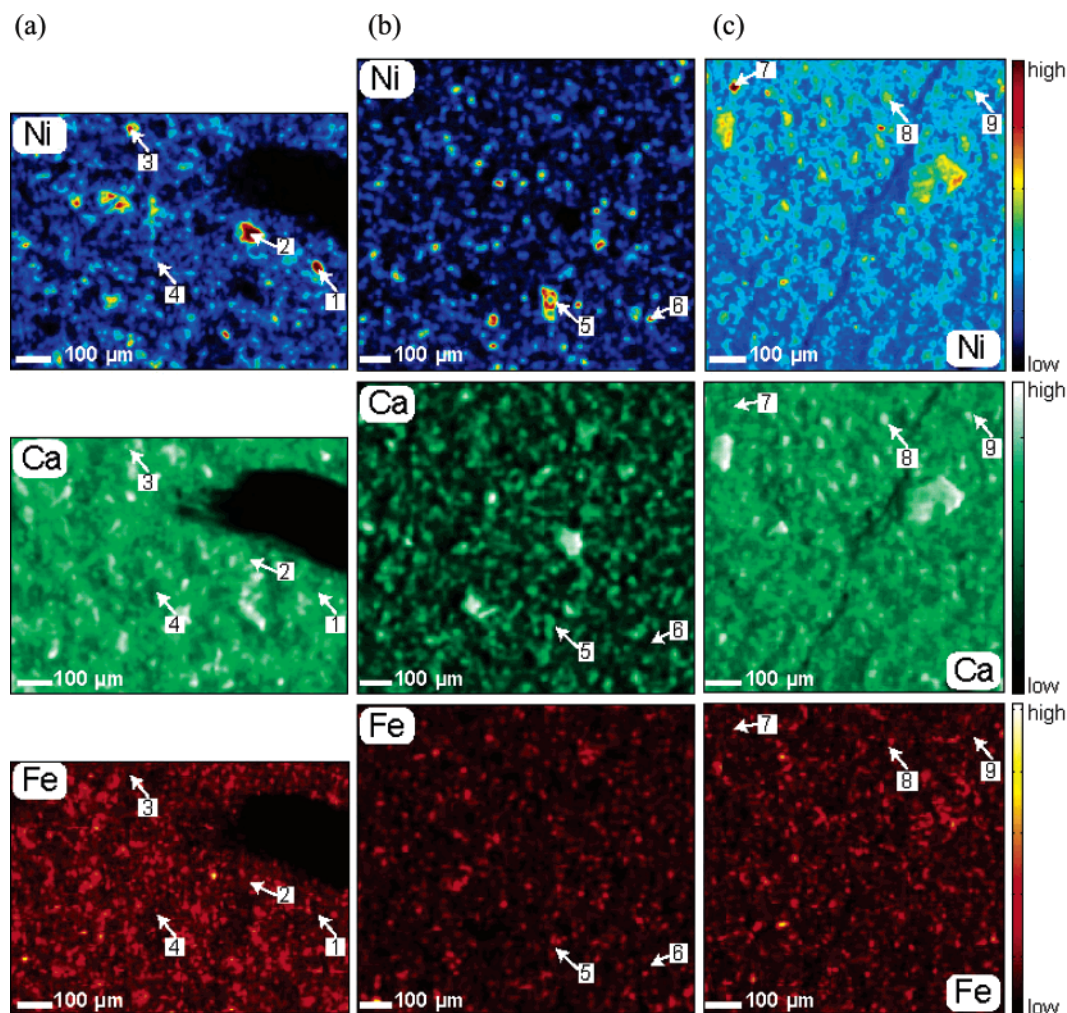
out. The Ni speciation was determined on various areas, herein referred to as ROI (region of interest) at both high and low Ni concentrated regions using  $\mu$ -extended X-ray absorption fine structure ( $\mu$ -EXAFS) spectroscopy.

Figure 4 shows selected  $\mu$ -EXAFS measurements collected at single regions together with the relevant reference spectra. The normalized, background-subtracted, and  $k^3$ -weighted  $\mu$ -EXAFS spectra of  $\text{Ni}(\text{NO}_3)_2$ -doped HCP samples with metal concentrations of 50, 500, and 5000 mg/kg and hydrated for 30 days are shown in Figure 4a. Most  $\mu$ -EXAFS measurements were performed on the HCP sample with the highest metal concentration (Ni<sub>cem\_5000</sub>). All  $\mu$ -EXAFS experimental spectra of this sample show similar features. The oscillation at  $\sim 4 \text{ \AA}^{-1}$  is broad, and its position is similar to that of the neoformed LDH phase, which forms upon Ni uptake by pyrophyllite (N-LDH) (Figure 4a). A small feature at  $\sim 5 \text{ \AA}^{-1}$  appears in the experimental spectra of ROI 1 and 3, which is well reproduced in both synthetic and neoformed Ni–Al LDH spectra. The beat pattern at  $\sim 8 \text{ \AA}^{-1}$  shows a splitting of the oscillation, which is better visible in the Fourier-backtransformed ( $\text{FT}^{-1}$ ) spectra (Figure 4c). Scheinost and Sparks (12) demonstrated that the beat pattern at  $\sim 8 \text{ \AA}^{-1}$  is an indication for the presence of Ni–Al LDH. In fact, this

beat pattern is observed in both Ni–Al LDH spectra, whereas the other reference compounds ( $\alpha$ - $\text{Ni}(\text{OH})_2$ ,  $\beta$ - $\text{Ni}(\text{OH})_2$ , and Ni-phyllsilicate) show an elongated upward oscillation ending in a sharp tip at  $\sim 8.5 \text{ \AA}^{-1}$ . Thus, the presence of the beat pattern at  $\sim 8 \text{ \AA}^{-1}$  together with the observed spectral features at  $\sim 4 \text{ \AA}^{-1}$  and  $\sim 5 \text{ \AA}^{-1}$  clearly indicate the presence of a Ni–Al LDH phase. These features appear in all collected spectra in the Ni-doped HCP sample with Ni concentrations of 5000 mg/kg.

The corresponding Fourier transforms (FT) of the  $k^3$ -weighted  $\mu$ -EXAFS spectra are shown in Figure 4b. The position of the first and second peak of the FT and the shape of the imaginary part reveal strong similarities with the Ni–Al LDH compounds. The amplitude of the second peak in the single experimental spectra is clearly reduced. This observation also applies for the Ni–Al LDH reference compounds but not for the other references (5, 12; see below). This finding further corroborates the presence of Ni–Al LDH at the Ni-rich regions in the Ni-doped HCP sample.

The structural parameters derived from multishell analysis ( $R + \Delta R$  range = 0.8–3.5  $\text{\AA}$ ) are summarized in Table 1. Data analysis reveals similar coordination numbers (CN) and



**FIGURE 3.**  $\mu$ -XRF elemental distribution maps of Ni, Ca, and Fe for the  $\text{Ni}(\text{NO}_3)_2$ -doped HCP samples with a water/cement ratio of 0.4, a hydration time of 30 days, and a final metal concentration of (a) 5000 mg/kg (the black region is silver, used as marker), (b) 500 mg/kg, and (c) 50 mg/kg. Selected regions for  $\mu$ -EXAFS/ $\mu$ -XANES measurements are marked 1–9. The color bar represents relative concentrations in each sample. Note that region 1 represents the Ni-rich rim in Figure 1, whereas region 2 represents the Ni-rich region shown in Figure 2.

interatomic distances ( $R$ ) for all investigated regions (Table 1, Table S2, Supporting Information). The first FT peak corresponds to an octahedral coordination of Ni with  $\sim 6$  oxygen atoms at 2.03–2.06 Å. The second FT peak reveals strongly reduced  $\text{CN}_{\text{Ni-Ni}}$  ( $\sim 3$ ) compared to  $\alpha$ - $\text{Ni}(\text{OH})_2$  ( $\sim 5$ ) and  $\beta$ - $\text{Ni}(\text{OH})_2$  ( $\sim 6$ ) (5). The  $\text{CN}_{\text{Ni-Ni}}$  of the experimental spectra are comparable to those determined for Ni–Al LDH. The  $\text{CN}_{\text{Ni-Ni}}$  is reduced as Ni is partly substituted by Al in Ni–Al LDH. This causes a significant destructive interference between Ni and Al EXAFS contributions, which results in an amplitude cancellation of the Ni and Al shells (5). Although the  $\text{CN}_{\text{Ni-Ni}}$  of the single ROIs of the Ni-doped HCP sample and Ni–Al LDH agree very well, the overall Ni–Ni distances (3.08–3.11 Å) are significantly longer than those in Ni–Al LDH (3.06–3.07 Å) (5). This finding suggests that, in addition to Ni–Al LDH, other Ni-containing phases are present. The longer  $R_{\text{Ni-Ni}}$  is attributed to the presence of  $\beta$ - $\text{Ni}(\text{OH})_2$  impurities ( $R_{\text{Ni-Ni}} = 3.13$  Å) (5).

**Influence of Varying Ni Concentrations.** The macro-spectroscopic study of Vespa et al. (5) demonstrated that, at a high Ni loading of 5000 mg/kg, a mixture of different Ni phases forms. Ni–Al LDH was found to be the predominant Ni species, which precipitates together with a small amount of  $\alpha$ - $\text{Ni}(\text{OH})_2$  and  $\beta$ - $\text{Ni}(\text{OH})_2$ . The above presented data from the same HCP sample shows that, on the microscale, mainly Ni–Al LDH forms together with small amounts of  $\beta$ - $\text{Ni}(\text{OH})_2$ .

The findings from the microscale investigations are in good agreement with the results from the macrospectroscopic study (5), indicating that the same Ni species form and, in particular, Ni–Al LDH is the predominant Ni phase in the cement matrix on both the macro- and microscale.

To address the question whether the findings from the Ni-doped HCP sample with 5000 mg/kg Ni loading can be extrapolated to samples with lower Ni concentrations, samples with 50 and 500 mg/kg Ni loadings have been investigated. The BSE images of the Ni-doped HCP samples with Ni concentrations of 50 and 500 mg/kg (Figure S1, Supporting Information) indicate that the microstructure of HCP is comparable to that of the sample with 5000 mg/kg Ni loading (Figure 1 and Figure 2). In fact, the Ni phases always form rims around the inner-C–S–H phase independent of the loading. The EDS analysis further reveals that Ni is not present in clinker minerals and hydrated cement phases (Table S1, analyses r and w, x indicated in Figure S1). In addition, the Ni concentrations on single Ni-rich spots on these rims vary only slightly between  $\sim 3$  and  $\sim 5$  wt % (Table S1, analyses s–v indicated in Figure S1) for the sample with 500 mg/kg and between  $\sim 1$  and  $\sim 3$  wt % (Table S1, analyses y and z indicated in Figure S1) for the sample with 50 mg/kg Ni loading. This indicates that, although the total Ni concentration in these samples is 10 and 100 times lower than in the Ni-doped HCP sample with 5000 mg/kg, the



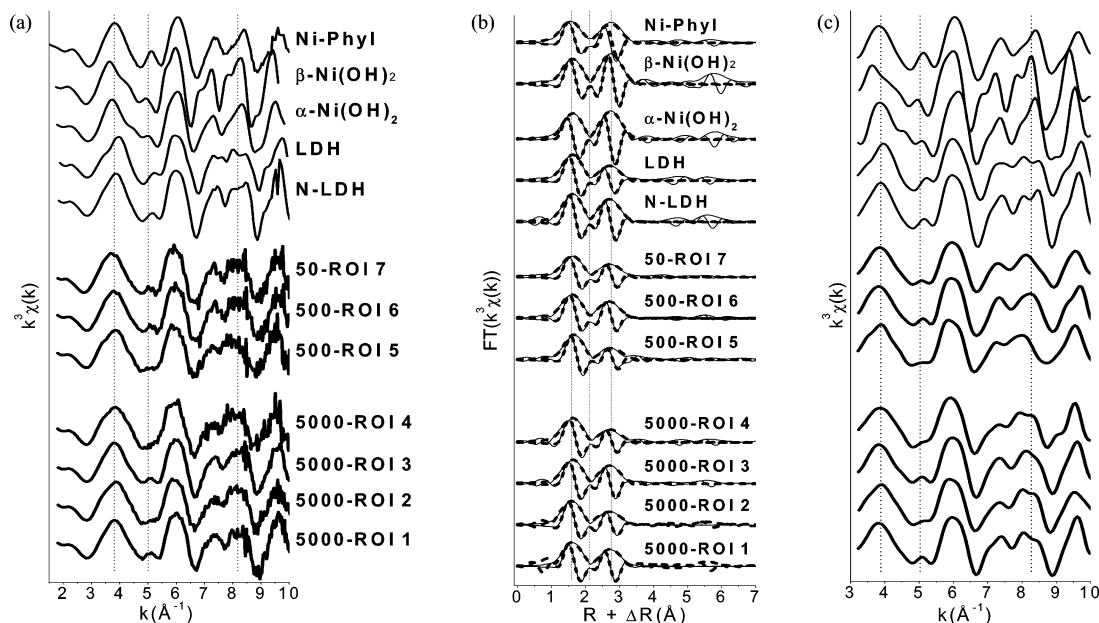


**FIGURE 4.** Ni K-edge spectra for Ni reference compounds and selected  $\mu$ -EXAFS experimental spectra of the  $\text{Ni}(\text{NO}_3)_2$ -doped HCP samples with a water/cement ratio of 0.4, a hydration time of 30 days, and three different total metal concentrations (50, 500, 5000 mg/kg). (a)  $k^3$ -weighted, normalized, background-subtracted spectra, (b) experimental (solid line) and calculated (dashed line) Fourier transforms (modulus and imaginary parts) obtained from the  $\mu$ -EXAFS spectra presented in a, (c)  $k^3$ -weighted EXAFS data for the Fourier-backtransform spectra obtained from Figure 4b ( $R + \Delta R$  range = 0.8–7 Å). Dotted lines indicate spectral features explained in detail in the text. Notations: ROI = region of interest, N-LDH = neoformed Ni–Al LDH, LDH = synthetic Ni–Al LDH (Ni:Al, 2:1 (δ)), Ni-Phyl = Ni-phyllsilicate.

**TABLE 1.** Structural Information Obtained from Selected  $\mu$ -EXAFS Ni K-Edge Data Analysis<sup>a</sup>

cement samples	Ni–O			Ni–Ni			$\Delta E_0$ (eV)	% res
	CN	$R$ (Å)	$\sigma^2$ (Å <sup>2</sup> )	CN	$R$ (Å)	$\sigma^2$ (Å <sup>2</sup> )		
Ni_cem_5000 (bulk-EXAFS) <sup>b</sup>	7.3	2.05	0.007	3.0	3.11	0.005 <sup>c</sup>	1.3	7.9
ROI 1	5.1	2.05	0.005	3.0	3.09	0.005 <sup>c</sup>	0.7	9.3
ROI 2	5.7	2.04	0.006	2.5	3.09	0.005 <sup>c</sup>	–1.9	6.1
ROI 3	4.7	2.05	0.003	3.2	3.09	0.005 <sup>c</sup>	0.2	9.2
ROI 4	6.6	2.06	0.007	2.3	3.10	0.005 <sup>c</sup>	–0.4	9.9
Ni_cem_5000 (bulk-EXAFS) <sup>b</sup>	5.3	2.05	0.005 <sup>c</sup>	2.3	3.12	0.005 <sup>c</sup>	0.0	9.0
ROI 5	5.3	2.08	0.005	2.0	3.12	0.005 <sup>c</sup>	3.2	11.6
ROI 6	6.2	2.05	0.007	2.9	3.07	0.005 <sup>c</sup>	–1.2	5.8
Ni_cem_5000 (bulk-EXAFS) <sup>b</sup>	6.3	2.04	0.005 <sup>c</sup>	1.8	3.17	0.005 <sup>c</sup>	–0.3	10.8
ROI 7	5.7	2.05	0.007	2.3	3.09	0.005 <sup>c</sup>	0.6	5.2

<sup>a</sup> Regions of interest, ROI, are indicated in Figure 3. <sup>b</sup> Vespa et al., 2006. <sup>c</sup> Fix parameters during fitting procedures.  $R$ , CN,  $\sigma^2$ ,  $\Delta E_0$  stand for interatomic distances, coordination numbers, Debye–Waller factors, and inner potential corrections. Estimated error:  $R_{\text{Ni–O}} \pm 0.02$  Å,  $\text{CN}_{\text{Ni–O}} \pm 20\%$ ,  $R_{\text{Ni–Ni}} \pm 0.02$  Å,  $\text{CN}_{\text{Ni–Ni}} \pm 20\%$ . %Res: deviation between experimental data and fit given by the relative residual in percent.  $N$  = number of data points,  $Y_{\text{exp}}$  and  $Y_{\text{theo}}$ : experimental and theoretical data points, respectively.

$$\% \text{ res} = \frac{\sum_{i=1}^N |Y_{\text{exp}}(i) - Y_{\text{theo}}(i)|}{\sum_{i=1}^N Y_{\text{exp}}(i)} \times 100$$

precipitation of a Ni phase still takes place. The BSE/EDS investigations were complemented with  $\mu$ -XRF measurements. The  $\mu$ -XRF distribution maps for the samples with 50 and 500 mg/kg Ni loadings indicate a heterogeneous distribution of Ni, Ca, and Fe as previously observed for the sample with the higher Ni loading (5000 mg/kg) (Figure 3). The Ni speciation was determined at selected Ni-rich regions in those samples using  $\mu$ -EXAFS. Figure 4 shows a comparison of the normalized, background-subtracted, and  $k^3$ -weighted EXAFS spectra (a), the FT (b), and the FT<sup>–1</sup> (c) for the various ROIs. The  $\mu$ -EXAFS spectra of the sample with 50 and 500 mg/kg are similar to each other and to the previously discussed  $\mu$ -EXAFS spectra of the sample with 5000 mg/kg. Data analysis reveals a first coordination shell with ~6 oxygen at  $R_{\text{Ni–O}}$  of 2.04–2.06 Å for all samples (Table 1). For the second coordination shell, CN is ~3, which is in good

agreement with  $\text{CN}_{\text{Ni–Ni}}$  in Ni–Al LDH. Bond distances for the second shell ( $R_{\text{Ni–Ni}}$ ) are determined to be 3.07–3.12 Å, which corresponds to distances previously determined for the sample with 5000 mg/kg Ni loading. This finding suggests that the composition of the Ni phases formed in Ni-rich regions is similar, regardless of the metal loading of HCP. Furthermore, the  $\mu$ -EXAFS results of the samples with 500 and 5000 mg/kg Ni loadings agree very well with the findings from the macrospectroscopic studies (5), indicating that the Ni-rich phases observed on the microscale are relevant to the whole matrix.

In the macrospectroscopic study, Vespa et al. (5) indicated that the Ni speciation was different for the sample with initial Ni concentration of 50 mg/kg. The study showed that the structural model used to analyze the data collected at increased Ni concentrations (>500 mg/kg) is not valid at the

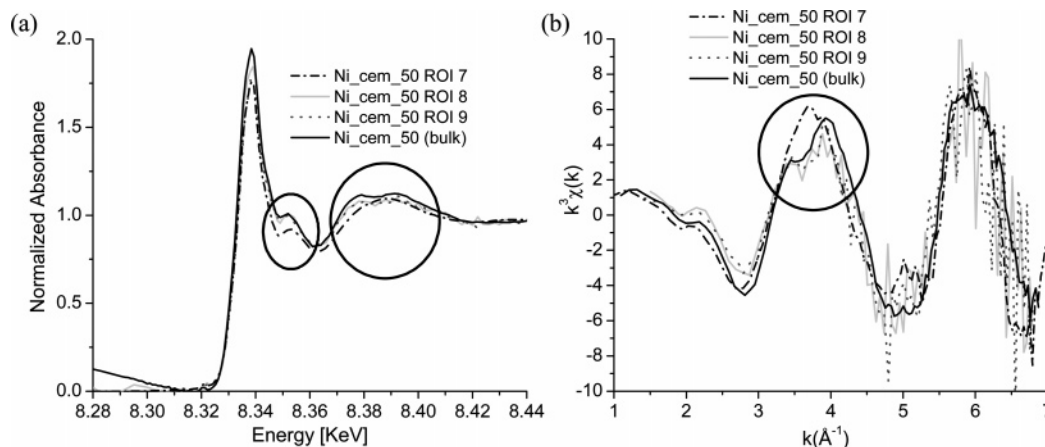


**FIGURE 5.** Ni K-edge  $\mu$ -XANES experimental spectra of ROIs (regions of interest) 7, 8, and 9 shown in Figure 3c of the  $\text{Ni}(\text{NO}_3)_2$ -doped HCP sample with a water/cement ratio of 0.4, a hydration time of 30 days, and a total metal concentration of 50 mg/kg. (a) Normalized absorbance, (b)  $k^2$ -weighted, normalized, background-subtracted  $\mu$ -EXAFS spectra. The powder experimental spectrum of the same sample (Ni\_cem\_50; (5)) is shown for comparison. Circles indicate spectral features explained in detail in the text.

lowest Ni concentration (50 mg/kg). In fact, the fit approach resulted in Ni–Ni distances longer (3.17 Å) than any known Ni compound (<3.13 Å). The  $\mu$ -EXAFS measurements aimed at investigating whether the Ni speciation deduced from the bulk-EXAFS on the 50 mg/kg Ni-doped HCP sample (5) can be discerned on the microscale. Figure 3c reveals a heterogeneous Ni distribution with Ni-rich and Ni-poor regions for the 50 mg/kg Ni-doped HCP sample. The  $\mu$ -EXAFS results of the Ni-rich ROI 7 (Figure 4; Table 1) indicate the formation of Ni–Al LDH, as discussed above. Thus, the results obtained for Ni-rich regions from the HCP sample at 50 mg/kg Ni loading are comparable with the results determined for the HCP samples at higher Ni concentrations. These findings suggest that Ni–Al LDH forms even in the HCP sample at 50 mg/kg Ni loading. However, the observation of Ni–Al LDH in the HCP sample at this low Ni concentration was not supported by the bulk-EXAFS measurements of the same sample (5). In latter studies, Ni–Al LDH was not the only species present in the cement matrix. To further discern the nature of the predominant Ni species in the 50 mg/kg Ni-doped HCP sample, Ni-poor regions were investigated. Because of the low metal concentration and the long acquisition time needed under these conditions, it was only possible to collect  $\mu$ -X-ray absorption near-edge structure ( $\mu$ -XANES) and  $\mu$ -EXAFS data up to 7 Å<sup>−1</sup> at Ni-poor regions of the cement matrix. Figure 5a shows normalized  $\mu$ -XANES spectra of ROIs 8 and 9 together with those determined for the Ni-rich ROI 7 (indicated in Figure 3c) and the corresponding bulk-XANES. The figure clearly reveals that the spectra collected at the Ni-poor ROIs 8 and 9 and the bulk-XANES data are comparable. However, the spectrum collected at the Ni-rich ROI 7 is different, showing two distinct features. The first feature is observed at 8350 eV. The second feature appears at 8390 eV, where the spectra of ROIs 8 and 9 show a splitting of the oscillation. This feature is also seen in the bulk-XANES spectrum and is clearly visible in the  $\mu$ -EXAFS spectra at  $\sim 4$  Å<sup>−1</sup> (Figure 5b). These findings suggest that at low Ni concentration at least two different Ni species are present. In strongly Ni-enriched regions (e.g., ROI 7), Ni–Al LDH forms, probably mixed with  $\beta$ -Ni(OH)<sub>2</sub>. At selected regions with significantly lower Ni concentrations (e.g., ROI 8 and 9), however, an additional Ni species is observed. This unknown Ni species is neither a Ni–Al LDH nor any other known Ni precipitate. Although the structural parameters of the species could not be identified in the present study, the species dominates in the cement matrix, as indicated from the previous bulk-EXAFS investigations (5).

## Acknowledgments

The staff of the Beamline 10.3.2/ALS of the SNBL and of the DUBBLE/ESRF is thanked for the experimental assistance during the synchrotron-based investigations. Thanks are extended to Dr. Curti, Kunz, and Dr. Harfouche for assistance during the measuring campaigns. Prof. Scrivener and Dr. Jenni from the IMX-EPFL and Brüttsch (LWV-PSI) provided measuring time and experimental assistance with the SEM/EDS investigations, and their contribution to the project is gratefully acknowledged. Dr. Johnson (EAWAG, Switzerland) is warmly thanked for the Ni–Al LDH reference compounds. Partial financial support was provided by the National Cooperative for the Disposal of Radioactive Waste (Nagra), Switzerland.

## Supporting Information Available

Table S1 shows various EDS analyses and Table S2 shows additional  $\mu$ -EXAFS results of the Ni-doped HCP samples. Figure S1 shows BSE images and the regions of the EDS analysis of two Ni-doped HCP samples with low Ni-loadings (500 and 50 mg/kg). This material is available free of charge via the Internet at <http://pubs.acs.org>.

## Literature Cited

- (1) Schmidt, M.; Beckefeld, P.; Götz, R.; Kamsties, S.; Kretz, C.; Molitor, N.; Neck, U.; Vogel, P. *Reststoff- und Abfallverfestigung. Immobilisierung von Schadstoffen-Recycling-Verbesserung der Deponiefähigkeit*; Expert Verlag: Renningen-Malmheim, 1995.
- (2) Chapman, N.; McCombie, C. *Principles and standards for the disposal of long-lived radioactive wastes*, 1st ed.; Elsevier Science, Ltd.: Oxford, U.K., 2003.
- (3) Glasser, F. P. In *Chemistry and microstructure of solidified waste forms*; Spence, R. D., Ed.; Lewis Publishers: Boca Raton, FL, 1993.
- (4) Scheidegger, A.; Wieland, E.; Dähn, R.; Spieler, P. Spectroscopic evidence for the formation of layered Ni–Al double hydroxides in cement. *Environ. Sci. Technol.* **2000**, *34*, 4545–4548.
- (5) Vespa, M.; Dähn, R.; Grolimund, D.; Wieland, E.; Scheidegger, A. M. Spectroscopic Investigation of Ni Speciation in Hardened Cement Paste. *Environ. Sci. Technol.* **2006**, *40*, 2275–2282.
- (6) Marcus, M.; MacDowell, A. A.; Celestre, R.; Manceau, A.; Miller, T.; Padmore, H. A.; Sublett, R. E. Beamline 10.3.2 at ALS: A hard-X-ray microprobe for environmental and material sciences. *J. Synchrotron Radiat.* **2004**, *11*, 239–247.
- (7) Ressler, T. WinXAS: A program for X-ray absorption spectroscopy data analysis under MS-Windows. *J. Synchrotron Radiat.* **1998**, *5* (2), 118–122.
- (8) Johnson, C. A.; Glasser, F. P. Hydrotalcite-like minerals ( $\text{M}_2\text{Al}(\text{OH})_6(\text{CO}_3)_{0.5}\text{XH}_2\text{O}$ , where M = Mg, Zn, Co, Ni) in the environment: synthesis, characterization and thermodynamic stability. *Clays Clay Miner.* **2003**, *51*, 1–8.

- (9) Lothenbach, B.; Wieland, E. A thermodynamic approach to the hydration of sulphate-resisting Portland cement. *Waste Manage.* **2006**, *26*, 706–719.
- (10) Peltier, E.; Allada, R.; Navrotsky, A.; Sparks, D. L. Nickel solubility and precipitation in soils: A thermodynamic study. *Clays Clay Miner.* **2006**, *54* (2), 153–164.
- (11) Taylor, H. F. W. *Cement Chemistry*, 2nd ed.; Thomas Telford: London, U.K., 1997.
- (12) Scheinost, A. C.; Sparks, D. L. Formation of layered single- and double-metal hydroxide precipitates at the mineral/water interface: A multiple-scattering XAFS analysis. *J. Colloid Interface Sci.* **2000**, *223*, 1–12.

*Received for review April 20, 2006. Revised manuscript received August 10, 2006. Accepted August 24, 2006.*

ES060957N